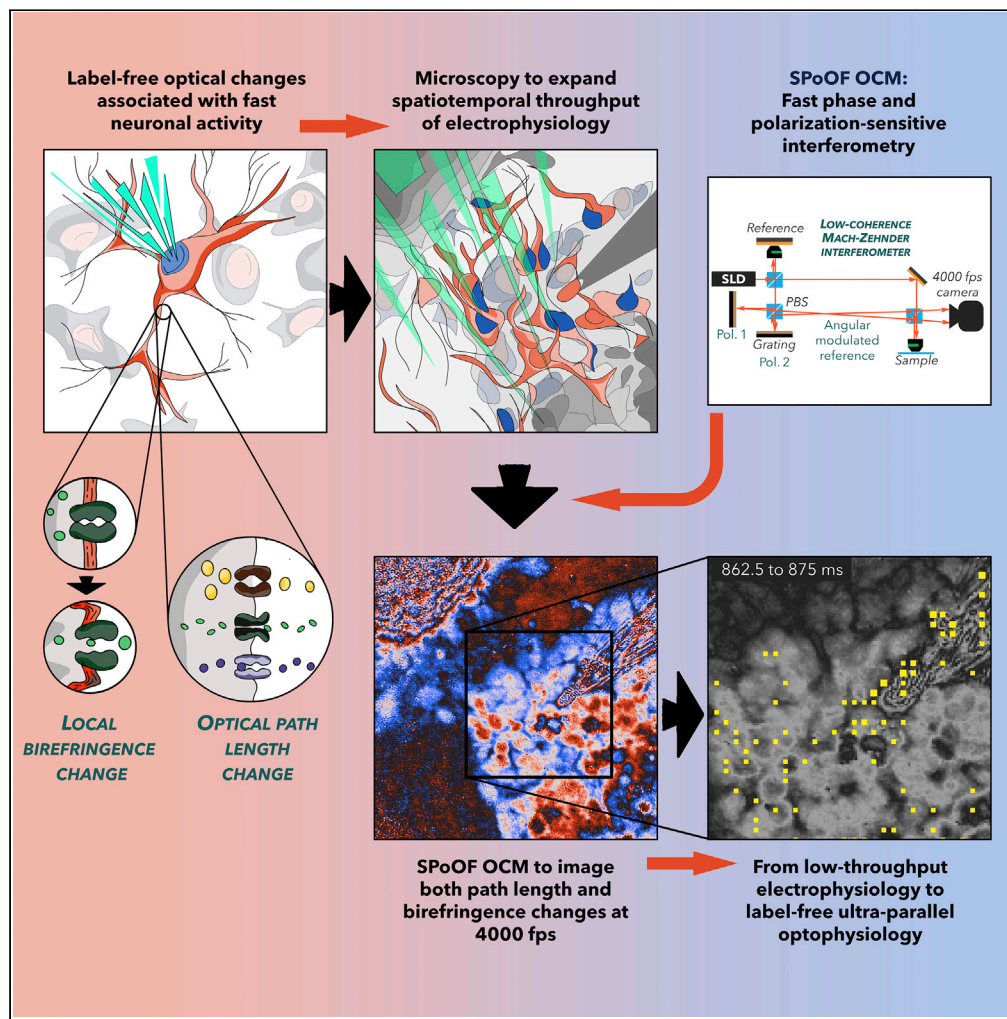## Article

Ultra-parallel label-free optophysiology of neural activity

Rishyashring R. Iyer, Yuan-Zhi Liu, Carlos A. Renteria, Brian E. Tibble, Honggu Choi, Mantas Žurauskas, Stephen A. Boppart

boppart@illinois.edu

Highlights

Changes to birefringence and optical path length are markers of neural activity

SPoOF OCM can capture both changes at 4,000 frames per second

Captures both single-cell and network-level neuronal responses at a millisecond scale

Optical measurements were compared against electrical ones and validated with tetrodotoxin

Article

Ultra-parallel label-free optophysiology of neural activity

Rishyashring R. Iyer,[1,2,7] Yuan-Zhi Liu,[1,6,7] Carlos A. Renteria,[1,3] Brian E. Tibble,[1] Honggu Choi,[1] Mantas Žurauskas,[1] and Stephen A. Boppart[1,2,3,4,5,8,*]

SUMMARY

The electrical activity of neurons has a spatiotemporal footprint that spans three orders of magnitude. Traditional electrophysiology lacks the spatial throughput to image the activity of an entire neural network; besides, labeled optical imaging using voltage-sensitive dyes and tracking Ca^{2+} ion dynamics lack the versatility and speed to capture fast-spiking activity, respectively. We present a label-free optical imaging technique to image the changes to the optical path length and the local birefringence caused by neural activity, at 4,000 Hz, across a $200 \times 200 \ \mu m^2$ region, and with micron-scale spatial resolution and 300-pm displacement sensitivity using Superfast Polarization-sensitive Off-axis Full-field Optical Coherence Microscopy (SPoOF OCM). The undulations in the optical responses from mammalian neuronal activity were matched with field-potential electrophysiology measurements and validated with channel blockers. By directly tracking the widefield neural activity at millisecond timescales and micrometer resolution, SPoOF OCM provides a framework to progress from low-throughput electrophysiology to high-throughput ultra-parallel label-free optophysiology.

INTRODUCTION

The efforts to scale up the throughput of the tools for neurophysiology have far-reaching consequences for our understanding of the neural circuit and the nervous system. However, engineering tools to observe the neuronal environment in its native state is challenging because neural activity patterns span over three orders of magnitude in both space and time. For both single-cell and network scales, neuronal activity can last anywhere between a few milliseconds, e.g., short spiking action potentials, to a few seconds, e.g., changes to the synaptic currents or responses of complex signaling cascades. The current flux in a single neuron is typically measured by inserting an electrode into or near the cell. The activity of neurons at a larger multicellular scale is inferred from blood flow patterns using fMRI. Although the former techniques have limited data throughput and provide little-to-no information about the overall network, the latter lacks the resolution to study the single-cell-scale mechanisms behind these neurological processes. Even multi-electrode arrays, which typically have hundreds of micron-sized electrodes in a grid pattern, have poor spatial resolution and limited spatial throughput. Optical microscopy has both the spatial resolution and field-of-view (FOV) to observe single-cell and network-level activity (Ji et al., 2016).

Most studies in optical imaging and neurophysiology have focused on engineering exogenous contrasts for functional fluorescence microscopy. Prevalent fluorescence markers include Ca^{2+} indicators that respond to activation of calcium ion channels, voltage or current sensitive dyes, and tags for synaptic vesicles (Carter and Shieh, 2015; Stosiek et al., 2003). Apart from exogenous agents for *in vitro* imaging, several transgenic animal models have been designed to express fluorescence markers for neurophysiology (Collot et al., 2019). However, fluorescence microscopy intrinsically requires relatively long exposure times per pixel which makes it challenging to image millisecond-scale dynamics at biologically safe optical beam powers. Several efforts have been made to improve the spatiotemporal throughput of fluorescence microscopy for neural imaging such as multiphoton excitation (Lecoq et al., 2019), multiple excitation beams (Wu et al., 2020), and light-sheet imaging (Voleti et al., 2019). Nonetheless, the versatility of the system is limited for fluorescence imaging techniques because they require modifications to the sample. The changes to the local biochemistry because of the contrast agents could also alter the functionality of the cells in the neural

microenvironment. In addition, light-sheet imaging requires transparent samples, and fast fluorescence imaging at kilohertz frame rates is restricted to a FOV that spans only a few tens of microns along each lateral axis (Voleti et al., 2019; Wu et al., 2020). Therefore, label-free optical microscopy has the versatility to image the functional states of neurons and the neuronal microenvironment at the necessary spatiotemporal scales. A prevalent technique for label-free imaging of neuronal activity involves optical coherence tomography (OCT) and optical coherence microscopy (OCM) for neural imaging (Akkin et al., 2007, 2009, 2010; Baran and Wang, 2016; Chen et al., 2009; Graf et al., 2009; Lazebnik et al., 2003; Li et al., 2020; Son et al., 2016; Strangman et al., 2002; Yeh et al., 2015; Zhang et al., 2020). As a natural extension of hemodynamic optical imaging in neuroscience (Li et al., 2020; Strangman et al., 2002), functional OCT and OCT angiography have been used to infer the neural activity indirectly (Baran and Wang, 2016; Son et al., 2016). However, blood flow is an indirect and slow measurement of neural activity. Local changes to the refractive index and birefringence because of ion flux are more sensitive to rapid neuronal activity. Indeed, Akkin et al. (Akkin et al., 2007, 2009, 2010) showed that individual action potentials could be measured from a single pixel using low-coherence interferometry. Individual action potentials can be discerned from the light scattered at large angles (Stepnoski et al., 1991) or by differential detection of the membrane displacements from brightfield microscopy (Yang et al., 2018). Even long-term changes to the cellular potential have been tracked by phase-sensitive interferometry (Batabyal et al., 2017; Hill et al., 1977; Marquet et al., 2014). Apart from changes to the refractive index, changes to the local birefringence also report neuronal activity (Badreddine et al., 2016; Carter et al., 2004; Koike-Tani et al., 2019; Lu et al., 2011). Studies have also found that changes to the birefringence are larger than the changes to the backscattered light because of axonal reorientation during changing membrane potentials, sometimes up to an order of magnitude (Foust and Rector, 2007). Most of these techniques are restricted to imaging a very limited FOV (single pixel-to-single-cell scale) or imaging slower dynamics. Full-field interferometry, quantitative phase imaging, and digital holographic microscopy have also been used to balance the spatiotemporal range of the measured scattered optical field (Hu et al., 2019; Larivière-Loiselle et al., 2020; Ling et al., 2018), with specific attention toward improving the phase stability and utilizing high-speed cameras.

Specifically, in this paper, the term neural activity has been used to denote the collective activity of the neural microenvironment and neuronal activity to denote the subset of neural activity pertaining to individual neurons rather than a collective. Unlike traditional electrophysiology, which is only sensitive to the electrical activity of cells, label-free optical microscopy responses are sensitive to all activities of a cell of which electrical activity is a part. Therefore, the extraction of the electrical activity of neurons using label-free optical microscopy requires validation with traditional electrophysiology measurements and biochemical modulation of the cellular currents.

We present a multimodal label-free optical microscope to image these intrinsic biomarkers of neuronal activity at the necessary spatiotemporal scales. We designed Superfast Polarization-sensitive Off-axis Full-field OCM (SPoOF OCM) that uses a 4,000 frames-per-second camera to image the spatial interference between the scattered field from neural cell cultures and a reference mirror at two different polarization states (Figure 1). The off-axis configuration obviates the need for any moving parts (Sudkamp et al., 2016) to ensure stability of 300 pm on filtered phase responses (Figure S1). The dual modulation arms utilize the spatial bandwidth of the setup effectively. Although several studies correlated changes to the OCM intensity and measured phase with neural activity, SPoOF OCM images the single-cell-scale neuronal activity in the entire FOV by tracking the scattering profile via changes to the intensity, the refractive index via the phase, and the birefringence via polarization-sensitive measurements. SPoOF OCM has more than twice the FOV compared to previous phase-sensitive widefield microscopy techniques for neuroimaging (Hu et al., 2019; Ling et al., 2018) in addition to measuring the polarization-sensitive responses and structural imaging. We demonstrate SPoOF OCM for imaging the spontaneous activity of differentiated neuroectodermal murine stem cells and the response of the neural circuit to electrical stimulation. The changes to the refractive index and birefringence of mammalian neurons cultured on a 2D surface measured using SPoOF OCM are consolidated into a single cumulative phase response metric and then compared with electrophysiology measurements. In addition, these measured optical responses are cross-correlated to discern the overall instantaneous correlation matrices. The optical responses measured using SPoOF OCM were validated to originate from current flow across fast ion channels by suppressing their electrical activity using tetrodotoxin (TTX) treatment. The dynamics of neural activity are visualized at a millisecond timescale and a micron spatial scale. SPoOF OCM establishes optical microscopy at kilohertz frame rates for ultra-parallel label-free imaging of neural activity and provides a framework for moving from invasive and low-throughput electrophysiology to label-free high-throughput optophysiology.
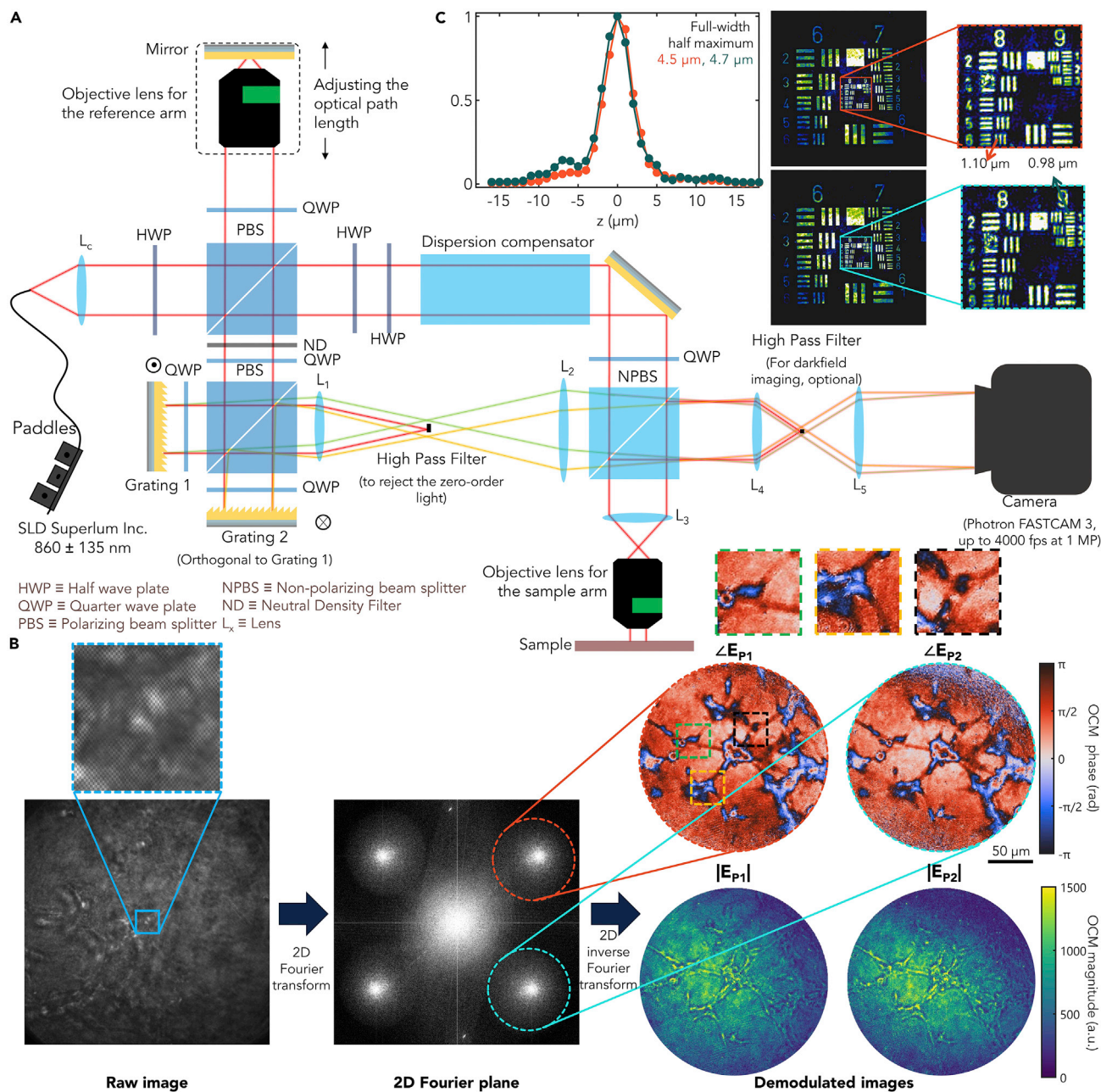
Figure 1. Design and characterization of SPoOF OCM

(A) System schematic for SPoOF OCM.

(B) Image reconstruction algorithm for SPoOF OCM to recover complex-valued OCM images. The zoomed-in raw images show the spatial modulation artifacts. The zoomed-in phase images show individual cells in the FOV.

(C) Axial and transverse resolutions of SPoOF OCM, where the orange and cyan plots represent $|E_{P1}|$ and $|E_{P2}|$, respectively. Scale bar: 50 μm.

RESULTS

Response of cells to electrical stimulation imaged using SPoOF OCM

Figure 2 depicts the responses of differentiated NE-4C neural cells (Schlett and Madarász, 1997) to electrical stimulation measured using SPoOF OCM (See STAR Methods and Figure S2 for details on the processing algorithms). Although the sample in Figure 1A had several sparsely distributed neurons to highlight the high-resolution structural imaging of the neuronal cell bodies, axons, and dendrites by SPoOF OCM, all samples presented henceforth contained a denser population of cells for efficient electrical stimulation
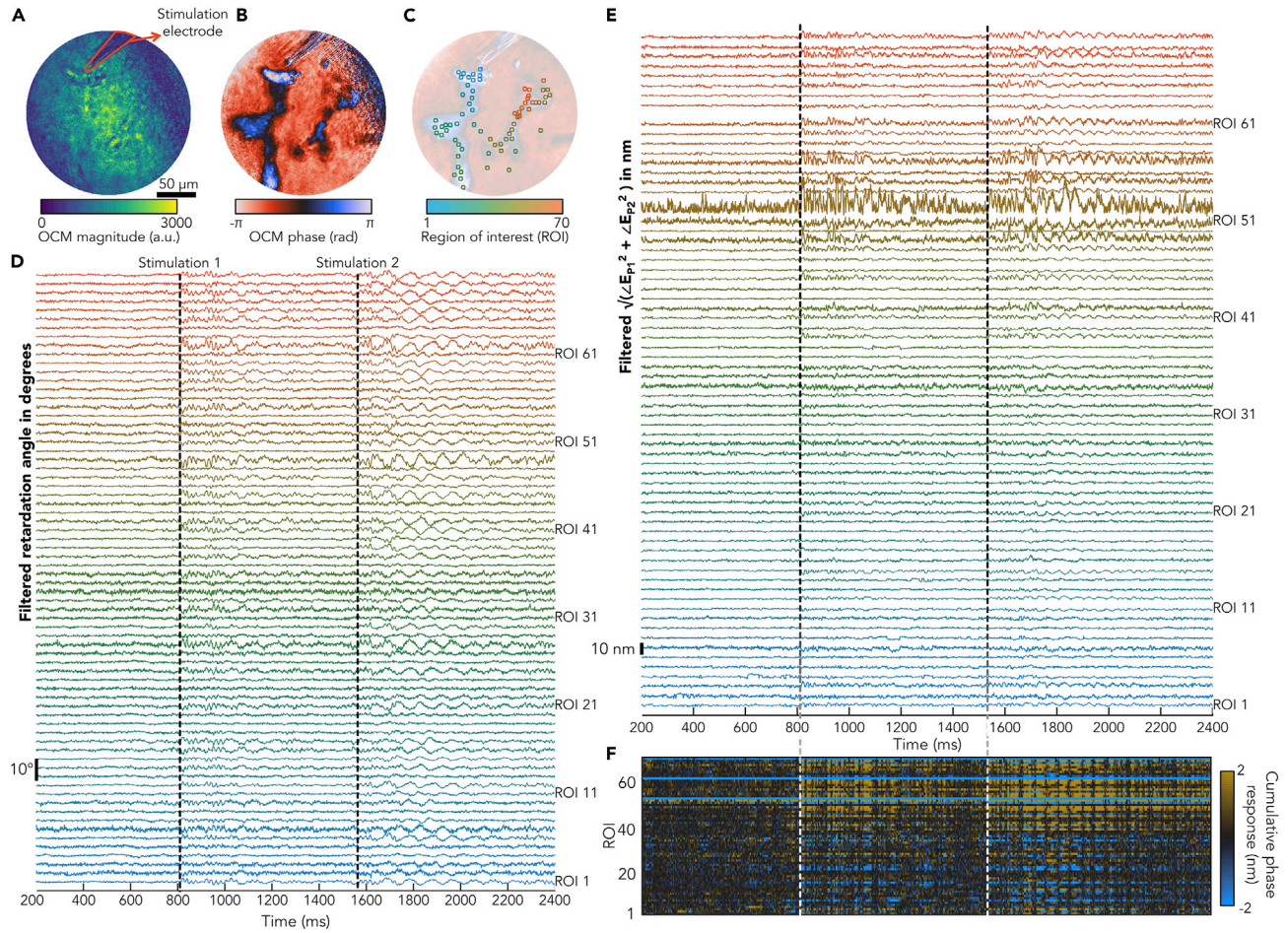
Figure 2. Imaging NE-4C neural activity using SPoOF OCM

(A) Intensity of the OCM images of NE-4C cells at P1.

(B) Phase of the NE-4C cells at P1.

(C) Phase of the NE-4C cells at P2, with the regions of interest overlaid. Scale bar: 50 μm.

(D) The retardation angle calculated as $\tan^{-1}(|iE_{P2} - E_{P1}|/|iE_{P2} + E_{P1}|)$ determines the qualitative polarization-sensitive response for each ROI in (C).

(E) The cumulative phase of the two polarization states, $\sqrt{\angle E_{P1}^2 + \angle E_{P2}^2}$ for each ROI in (C).

(F) The response that was shown in (E) depicted as a chart. (See Figure S4).

and easier field-potential measurements from multiple cells at once. Two main clusters can be observed in Figures 2A–2C, where several regions of interest (ROIs) were chosen near the center of cellular structures. The ROIs were sorted based on the cluster and their proximity to the electrode tip. The electrode tip is apparent near ROIs one to five and the axon connection between the two large clusters in the FOV is apparent near ROIs 11, 13, and 48. Several measurements from SPoOF OCM could be used to detect neuronal activity. Based on the Jones matrices of the optical setup, the detected OCM signals, E_{P1} and E_{P2}, can be described as

$$\begin{bmatrix} E_{P1} \\ E_{P2} \end{bmatrix} = \sqrt{R(z)} J_{\text{Sample}}(\delta_s, \theta_s) J_{\text{Sample}}(\delta_s, \theta_s) J_{\text{QWP}}\left(\frac{\pi}{2}, \frac{\pi}{4}\right) J_{\text{HWP}}(\pi, 0) J_{\text{HWP}}(\pi, 0) \begin{bmatrix} 1 \\ 0 \end{bmatrix},$$

$$= \frac{-\sqrt{R(z)}}{\sqrt{2}} \begin{bmatrix} \cos\delta_s + i\, e^{2i\theta_s} \sin\delta_s \\ i\cos\delta_s + e^{2i\theta_s} \sin\delta_s \end{bmatrix}$$

(Equation 1)

where J_{Sample}, J_{HWP}, and J_{QWP} are the Jones matrices for the sample, half-wave plate, and quarter-wave plate, respectively, R is the reflectivity of the sample, θ_s is the orientation angle, and δ_s is the retardation angle. Based on this, the retardation angle could be derived as

$$\delta_s \;=\; \tan^{-1}\left(\frac{|iE_{P1} - E_{P2}|}{|iE_{P1} + E_{P2}|}\right). \tag{Equation 2}$$

This polarization-sensitive response is shown in Figure 2D, where most ROIs are inactive before the moment of electrical stimulation delivered through the electrode, i.e., before 805 ms, after which the individual regions show distinct undulations. A second stimulation was imparted at 1550 ms. Undulations to the retardation angle are apparent after both stimulations. However, these undulations appear to be unlike the spiking activity expected from neural responses. This can be attributed to the lower intensity stability compared to the phase stability (Figure S1), the polarization noise of the light source, and the calculation of a fractional element in the estimation for the arctangent. In addition, the tangent function is ill-conditioned near the asymptotes. Furthermore, as seen in Figure S3, although the phase difference between P1 and P2 remains constant during calibration with a quarter-wave plate for experimental evaluation of the Jones matrix of the sample, the modulation to the intensity does not appear to match with the theoretical expectations. Instead, if the phases of the two detected OCM signals, $\angle E_{P1}$ and $\angle E_{P2}$, which are ideally shifted by $\pi/2$, are assumed to form a Cartesian plane, then the cumulative phase response can be estimated as the Euclidian distance from the origin estimated as $\sqrt{\angle E_{P1}^2 + \angle E_{P2}^2}$. This is expected to have a higher sensitivity compared to estimating δ_s at the cost of sacrificing the ability to quantify the birefringence of the sample. However, as seen in the responses in Figure 2E, just the phase can detect sharp and distinct spikes of varying widths and amplitudes. These spikes appear to have a typical magnitude of 0.5–20 nm, similar to previously reported values (Yang et al., 2018). Interestingly, cells in ROIs 2, 4, 52, etc., in Figure 2E appear to be active even in the absence of any stimulation. However, the other cells are mostly inactive before the moment of stimulation, after which the individual regions show pronounced responses. In contrast, ROIs 5, 6, 19, 63, etc., in Figure 2E do not show any obvious responses even after electrical stimulation. Because ion flux is abundant in any functionally active *in vitro* model, the observed phase responses contain both spiking activity and long-term phase responses. Although the ridge plots in Figures 2D and 2E highlight the individuality of each response, the response chart in Figure 2F helps for observing the correlation between the responses from the ROIs qualitatively. They demonstrate the coordination between the different ROIs both in the amplitude difference and the phase plots. Interestingly, the responses are sustained through 1100 and 1400 ms, albeit weaker even in the absence of stimulation observed in the charts.

Quantitatively, similar to the methods implemented previously (Renteria et al., 2020; Voleti et al., 2019), the correlation coefficient and the lag/lead times between two responses can be calculated from Equation (3), where S_n is the signal from region of interest n, C_{mn} is the cross-correlation between S_m and S_n, r_{mn} is the normalized correlation coefficient, and $\tau_{lag_{mn}}$ is the lag or lead of region n compared to m.

$$C_{mn}(\tau) = S_m(t) \otimes S_n(t), \; n < m,$$

$$r_{mn} = \frac{\int C(\tau)}{C(\tau = 0)}, \; \text{and} \tag{Equation 3}$$

$$\tau_{lag_{mn}} = \underset{\tau}{\mathrm{argmax}}|C(\tau)|.$$

The result of this analysis for the responses shown in Figure 2D is shown in Figures 3A–3C, in matrix format, and as an accompanying pictorial representation showing the response correlation matrix, where S_m and S_n correspond to δ_s. The response correlation matrix has been previously used to describe connectivity patterns in neural networks (Renteria et al., 2020; Voleti et al., 2019). Tracking the correlation matrices highlights that the electrical stimulation of neurons not just activates a localized region, but the overall network, as observed in the increased correlation (Figure 3A) and sudden onset of connections (Figure 3C) between 800 and 1100 ms and again between 1500 and 1700 ms. The sustained neural activity gradually decreases between 1100 and 1400 ms and eventually returns to rest between 1400 and 1500 ms. In addition, immediately after the stimulation at 805 ms, all responses appear to have negligible lag and lead times but the sustained neural activity patterns, especially between 1000 and 1200 ms, show increased lag and lead times corresponding to the natural rhythm of the neural circuit (Figures 3B–3C). The time-varying correlation matrices for the responses in Figure 2E are shown in Figure S4, where S_m and S_n in Equation (3) correspond to the cumulative phase response. The results in Figures 2 and 3 show that the neural activity of individual ROIs and the overall correlation matrices could be measured using changes to the birefringence and the undulations to the phase represented as a cumulative phase metric. These results also establish that SPoOF OCM can measure neural activity in response to electrical stimulation.
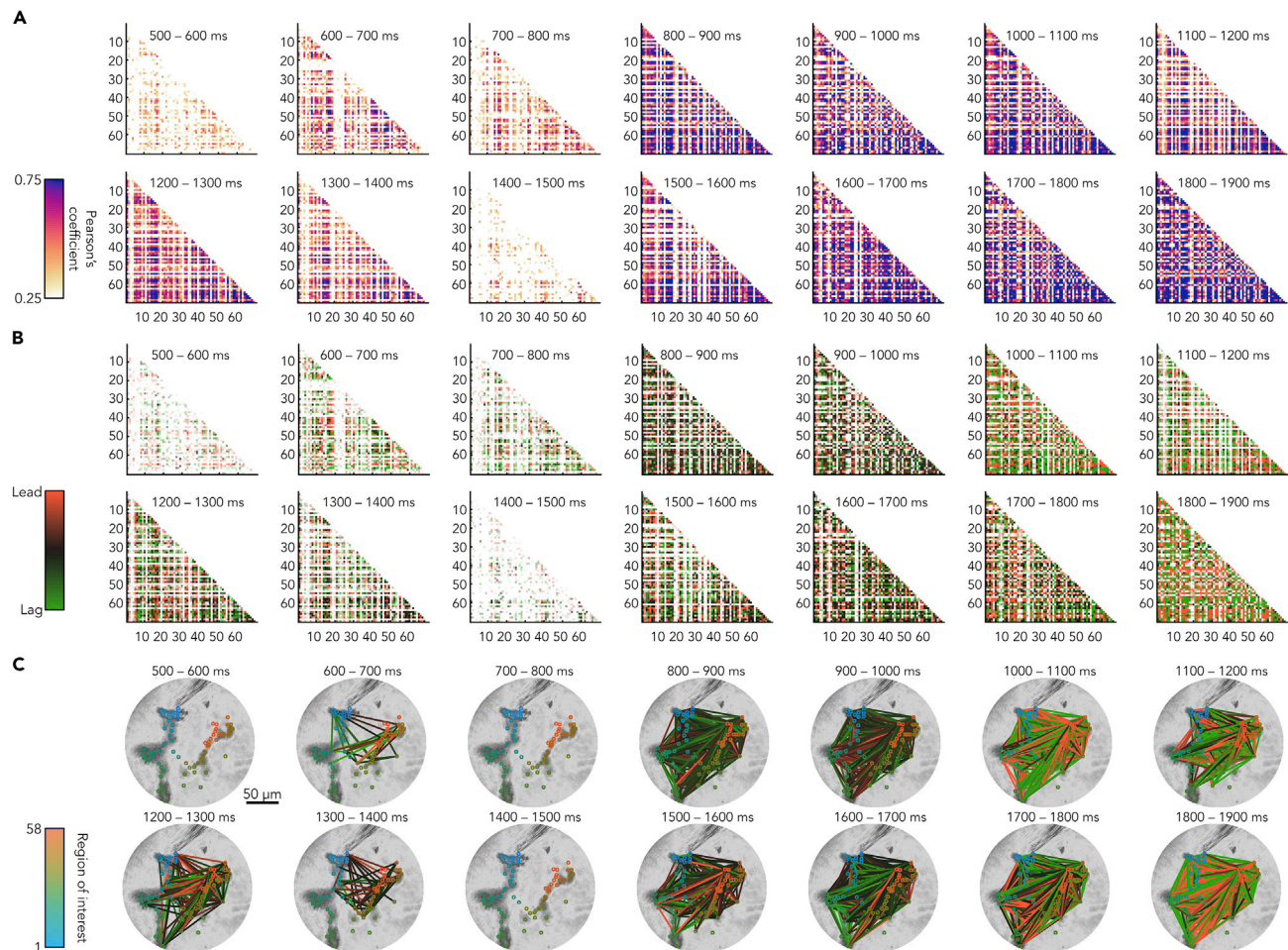
Figure 3. Neural connectivity determined from SPoOF OCM responses

(A) The cross-correlation matrix of the retardation angle responses in Figure 2D.

(B) The lag matrix derived from cross-correlating the responses from different regions of interest. The transparency depicts the correlation coefficient. The *x* and *y* axes of the matrices in (A) and (B) correspond to the ROIs in Figure 2A.

(C) The images pictorially depict connectivity between the different regions of interest with a correlation coefficient >0.6 and where the SD of each response in the 100-ms window must be greater than the SD of the whole 2500 ms. The connectivity maps are overlaid on the phase of the OCM image at polarization P1. Scale bar: 50 μm. (See Figures S5 and S6).

Spontaneous activity of neurons imaged with SPoOF OCM and validated with electrophysiology

Electrical stimulation evokes obvious and large responses from neurons. However, the goal of a reliable neurophysiology setup must be to detect both spontaneous and stimulated activity of neurons and correlate these optical measurements with their electrical activity. We utilized an electrophysiology setup capable of field potential measurements to compare the optical responses with the electrical activity of neurons. Figure 4 shows the spontaneous activity of differentiated NE-4C neurons measured using SPoOF OCM. Similar to the ROIs selected in Figures 2A–2C, ROIs were chosen by observing the cell structures and sorted based on their proximity to the electrode tip (Figure 4A). Individual cells can be identified visually, and the dendritic connections are apparent, especially at the edge of the neuronal structures where phase-wrapping is minimal. The phase responses of the two polarization states were collectively calculated as $\sqrt{\angle E_{P1}^2 + \angle E_{P2}^2}$ and are shown in Figure 4B. The response from estimating the retardation angle is shown in Figure S5, which seems subdued because of lower sensitivity for estimating the quantity. The response of each ROI appears to be unique and distinctly different from neighboring ROIs. Nonetheless, several prominent responses can be tracked across several ROIs visually, especially in the features
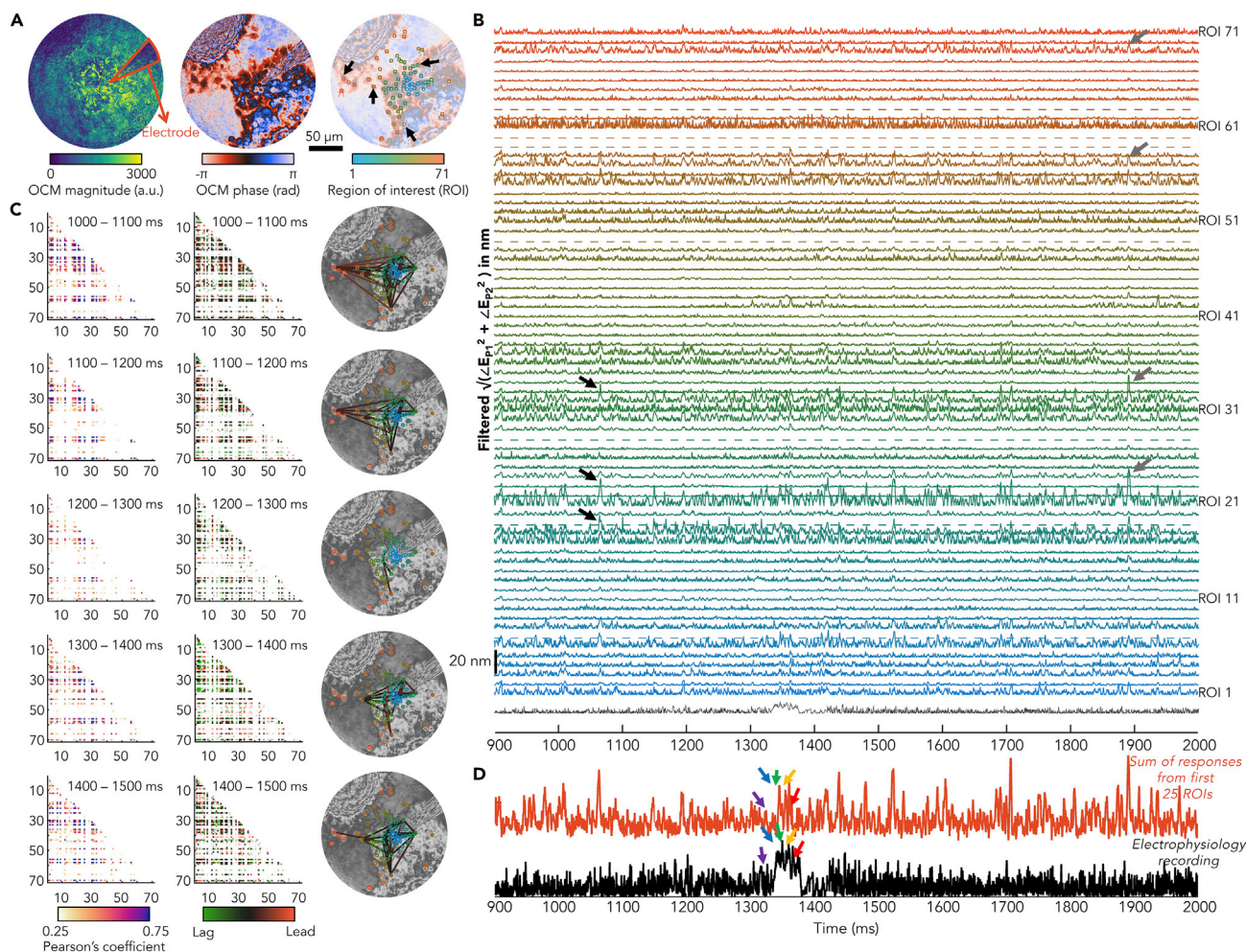
Figure 4. Spontaneous activity of NE-4C cells

(A) Complex-valued SPoOF OCM images at both polarization states. The regions of interest are sorted by their proximity to the electrode tip. The black arrows indicate the hubs of connectivity based on the results in (C) Scale bar: 50 μm.

(B) Cumulative phase calculated as $\sqrt{\angle E_{P1}^2 + \angle E_{P2}^2}$ for the 71 ROIs chosen in the sample. The responses in the ridge plot were converted to nanometers. The electrophysiology measurement is shown in black.

(C) The correlation coefficient matrix and the lag matrix derived from cross-correlating the responses from different regions of interest. The transparency depicts the correlation coefficient. The images pictorially depict connectivity between the different regions of interest with a correlation coefficient >0.6 and where the SD of each response in the 100-ms window must be greater than the SD of the whole 2500 ms.

(D) The sum of the first 25 responses in orange compared against the electrical recordings. The arrows indicate the spikes that are apparent both in the summed responses and the electrical recordings.

indicated by the black and gray arrows. Such correlations from these responses were quantified in Figure 4C using Equation (3) and the response correlation matrices within a 100-ms window were calculated. Several hubs of activity can be recognized in these matrices, indicated by the black arrows in Figure 4A. The complete series of correlation matrices are shown in Figure S6. The expression of voltage-dependent inward Na$^+$ currents (I_{Na}), fast-acting A-type K$^+$ currents (K$_A$), and delayed outwardly rectifying K$^+$ currents (K$_{DR}$) in differentiated NE-4C cells (Anděrová et al., 2006) further validate the characteristics of the observed spiking activity observed using SPoOF OCM.

The spontaneous activity of neurons was also compared against the electrical measurements. In Figure 4B, an instance of prominent membrane depolarization is observed between 1300 and 1400 ms. Correspondingly, spikes in the phase responses are apparent in several ROIs, indicated by the arrows in Figure 4A. Because the electrical measurements are field-potential recordings, the responses from the 25 ROIs closest to the electrode were summed together and shown in Figure 4D for visual comparison. Although the
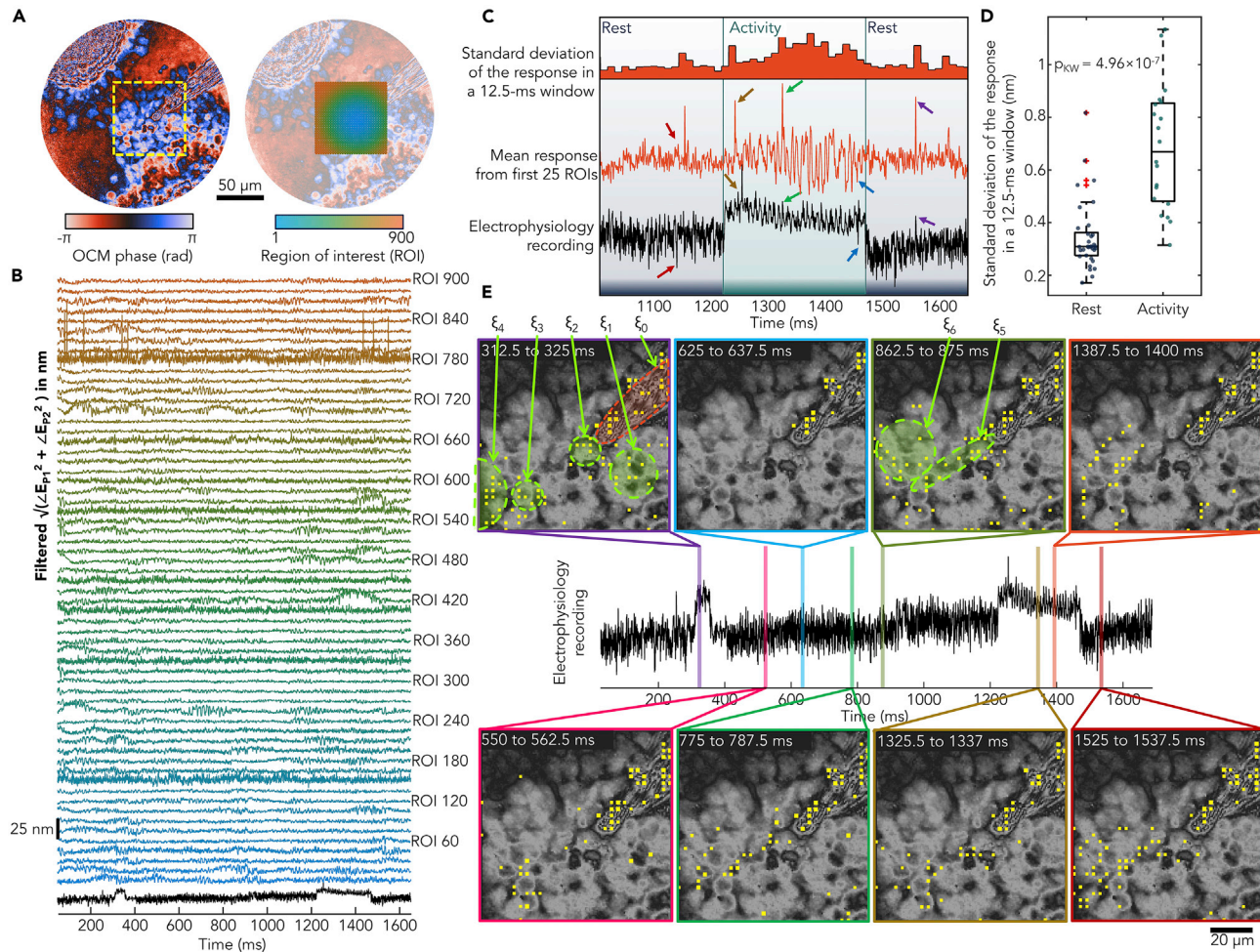
Figure 5. Widefield optical imaging of neural activity

(A) Phase of the SPoOF OCM images at both polarization states with the regions of interest sorted by the proximity to the electrode tip overlaid on the phase of P2. The 900 5 × 5 pixels² ROIs were chosen evenly spaced in a 75 × 75 μm² region. Scale bar: 50 μm.

(B) Phase response of every 15th ROI, calculated as $\sqrt{\angle E_{P1}^2 + \angle E_{P2}^2}$ in nm, and the electrophysiology measurement (in black).

(C) The sum of the first 25 responses in orange compared against the electrical recordings. The arrows indicate the spikes that are apparent both in the summed responses and the electrical recordings. The SD of the phase response is calculated for every 12.5-ms window and shown in the bar graph. The periods of activity (cyan) and rest (blue) were chosen based on the electrophysiology response.

(D) Comparison of the standard deviations during the activity (1220–1480 ms) and resting (otherwise) periods for the response shown in c, calculated over a 12.5 ms window, where the p value was estimated using a Kruskal-Wallis test (N = 50). The line inside each box is the median and the top and bottom edges of each box are the upper and lower quartiles, respectively.

(E) The filmstrip of spiking activity (yellow dots) overlaid on the phase responses calculated as any SD of the filtered phase responses of the ROIs in a 12.5-ms window over 2 nm, shown for selected intervals indicated on the electrophysiology plots. The regions, ξ_{0-6}, indicate hubs of activity at different instances. Scale bar: 20 μm.

electrode recordings show a narrow view into the neural activity, the optical response provides a spatial context to the electrical activity of neurons.

Widefield optical imaging of neural activity

To effectively utilize the spatiotemporal output of SPoOF OCM and to demonstrate ultra-parallel opto-physiology, we chose 900 linearly spaced ROIs in a 75 × 75 μm² region while observing the spontaneous activity of NE-4C neurons (Figure 5A). The neuronal activity was estimated as the cumulative phase of the two polarization states. The phase responses of every 15th ROI, along with the field potential measurements, are shown in Figure 5B, where the undulations appear to be synchronized in several ROIs corresponding to the spiking activity in the electrical measurements. The long train of spiking activity between

1220 and 1480 ms is specifically highlighted in Figure 5C and compared against the response from the 25 ROIs closest to the electrode tip. First, similar to Figure 4D, the distinct spikes in the electrophysiology measurements have counterparts in the optical responses, as highlighted by the arrows. Second, during the train of spiking activity between 1220 and 1480 ms, the undulations in the optical responses become larger. This would correspond to an instantaneous increase to the SD in a local temporal window as shown in the accompanying bar graph. The SD of each ROI was calculated for every 12.5 ms window between 1 and 1700 ms. As seen in Figure 5D, when calculated for the optical response shown in Figure 5C, the standard deviations during neural activity, i.e., during the period of depolarization observed on the electrophysiology graph, are significantly higher compared to the standard deviations before and after this instance. NE-4C cells have also been shown to have persistent passive conductance after differentiation (Jelitai et al., 2007). However, because we wished to extract the millisecond-scale activity, we chose a temporal window of 12.5 ms. Therefore, our optical measurements in Figures 5C–5E are associated with the fast spiking activity of the neurons, typically attributed to the voltage-dependent channels- I_{Na}, K_A, and K_{DR}. Based on Figure 5D, a conservative estimate of any SD over 1 nm was counted as an event of neuronal activity and is shown for each frame in Video S1 along with the electrical measurements at the same time. Eight specific frames are shown in Figure 5E to highlight the neural activity at different regions in the sample. The region encompassing the electrode is indicated by ξ_0 whose displacement could be because of instability in mounting and not corresponding to the electrical activity. During the first instance of depolarization between 300 and 400 ms, the regions ξ_{1-4} appear to be activated, where ξ_{2-3} correspond to individual cells. The responses at ξ_3 are also apparent between 550 and 562.5 ms, corresponding to the activity of the single cell in the region. Interestingly, at different instances, the neural activity appears to propagate along ξ_5 from/to regions ξ_4 and ξ_6, especially during the spike train between 1220 and 1480 ms. This is further confirmed by observing the activity pattern between 1187.5 and 1200 ms in Video S1, where the activity is confined to the neural cell bodies in regions ξ_3, ξ_4, and ξ_6, which then propagates along ξ_5 toward the electrode tip. The onset of activity at ξ_3, ξ_4, and ξ_6 precedes the onset of depolarization in the electrophysiology recording by approximately 25 ms, which suggests the origin and directionality of this activity pattern. The presence of K_{DR} channels in differentiated NE-4C cells (Anděrová et al., 2006; Jelitai et al., 2007), which allow a sustained K^+ efflux with a delay after membrane depolarization and play a critical role in neurotransmission (Yost, 1999), could account for this delay.

Validation of electrical activity measured using SPoOF OCM using Na⁺ channel blocker

To validate that the SD of the cumulative phase response was because of currents through fast ion channels, the experimental scheme established in the previous section was used to image the activity of NE-4C neurons after suppressing the Na^+ channels using 100 nM TTX. Having shown that the instantaneous SD over a 12.5 ms window was an appropriate activity metric that corresponded well with the electrode measurements, the same scheme was adapted to calculate the activity within 900 evenly spaced 5×5 pixels^2 ROIs chosen within a 75×75 μm^2 region in the samples with and without TTX. For active neurons that have sporadic spontaneous electrical activity, both the mean and variance of this activity metric are expected to increase. Therefore, both parameters were calculated for each ROI cumulatively over the entire dataset and shown in Figure 6A, where these differences could be visually observed. A transparency map was overlaid to focus on the cell bodies and not the background. More pixels in the control group appear to have a higher mean value of the activity metric compared to the TTX group. Similarly, the samples in the TTX group have visibly and uniformly lower variance of the activity metric compared to the control group. Estimating the ratio between the variance and mean improves the visual contrast between the two groups. This was quantitatively analyzed for every 1 s duration within the acquisition window, where the light orange (TTX) and light blue (control) contours form two distinct groups (Figure 6B). Cumulatively, the contours in dark orange and blue, corresponding to all ROIs of the TTX group and control group for all datasets estimated for every 1 s interval, respectively, have significantly ($p \ll 0.005$) different distributions across both axes. Owing to the inhibitory effect of TTX, both the mean and variance of the activity metric are lower for the TTX group. The overlap between the two groups can be explained by spatial regions that remain silent in the control group during the 1 s interval. As further validation, the responses of the same FOV before and after the addition of TTX are shown in Figure S7, which has a similar trend to the results in Figure 6. Nonetheless, this demonstrates that the metric designed to extract widefield neural activity using SPoOF OCM is sensitive to the activity of the cation channels in these neurons and that SPoOF OCM can track the electrical activity of neurons at a millisecond timescale and with a micron spatial scale over several seconds and hundreds of microns, label-free.
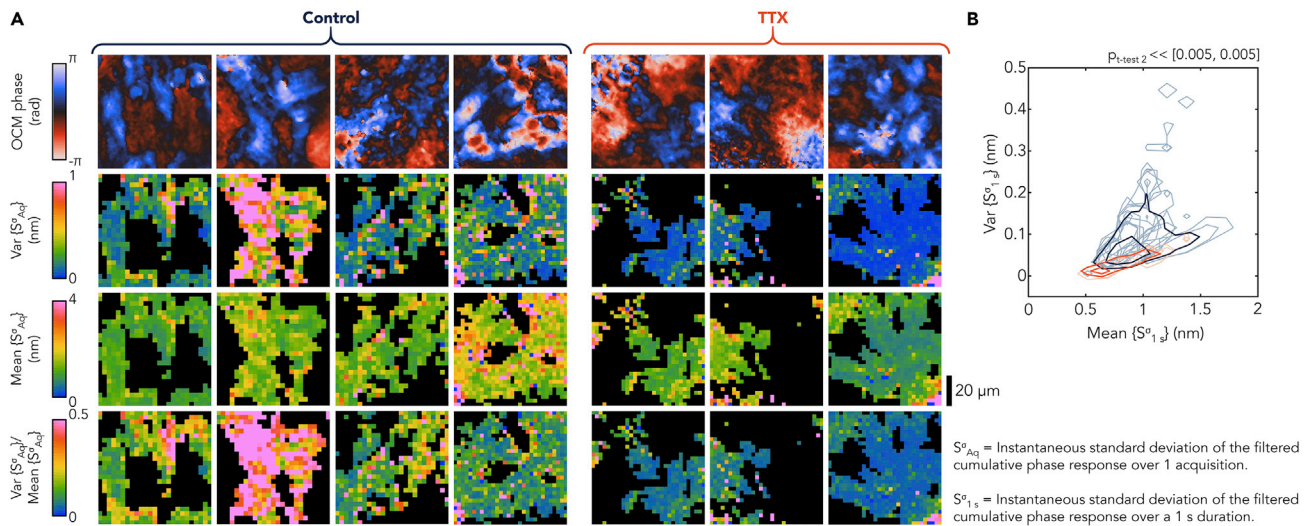
Figure 6. TTX suppression of spontaneous neural activity measured with SPoOF OCM

(A) Phase of the SPoOF OCM images of P2 (Row 1), variance and mean of the instantaneous SD of the cumulative phase response in nm (within a 12.5-ms window) calculated over the entire dataset in nm for 900 5 × 5 pixels^2 ROIs chosen evenly spaced in a 75 × 75 μm^2 region (Row 2 and 3, respectively), and the ratio between the variance and the mean in rows 2 and 3 (Row 4), for different samples treated with 100 nM TTX (or the cell culture media for control) for 20 min at 37°C before imaging. Scale bar: 20 μm.

(B) Contour plots of the variance and mean of the instantaneous SD of the cumulative phase response in nm (within a 12.5-ms window) calculated over 1-s durations in light blue (control) and orange (TTX), and after cumulating all the 5 × 5 pixels^2 ROIs for all samples in each group in dark blue (control) and orange (TTX). ($N_{control}$ = 4 dishes/acquisition datasets, 16 1-s acquisition intervals, 6684 ROIs; N_{TTX} = 3 dishes/acquisition datasets, 6 1-s acquisition intervals, 2,372 ROIs; p values were estimated from the two-sample t-test; the two levels for the contour were chosen automatically by the plotting software) (See Figure S7).

DISCUSSION

The individual components of SPoOF OCM and our choice of using changes to the optical path length and birefringence as markers of neural activity were motivated by previous studies. Off-axis full-field imaging has been previously used to track the phase changes because of neural activity, albeit at a lower frame rate and transmission geometry (Hu et al., 2019). The long-term phase changes because of optical stimulation of transgenic neurons were shown to be sustained over several seconds. On a millisecond timescale, previous studies on wide-field phase-sensitive neural imaging, demonstrated by Ling et al. (2018), could track the action potential propagating across a single cell with an effective frame rate of 1 kHz on genetically modified HEK-293 cells. However, although the HEK-293 cells have been widely used to simulate neuronal responses, they are significantly larger compared to the NE-4C neurons. Therefore, few cells can be observed in the FOV. Yang et al. showed that the membrane displacement could be tracked along a single axon from a mammalian neuron at 1600 Hz for a single cell in the FOV by tracking the changes to the intensity (Yang et al., 2018). Previous studies for imaging the changes to birefringence at a millisecond timescale were restricted to a smaller FOV and relied on transmission mode (Ling et al., 2018). SPoOF OCM consolidates the advantages of each component, namely phase-sensitive and polarization-sensitive imaging at kilohertz frame rates, into a single framework. Compared to low-coherence interferometry, SPoOF OCM could image the neural activity on a 2D plane rather than along a single line. In addition, the depth-resolved imaging capability of SPoOF OCM offers several advantages. First, decoupling the axial and transverse resolutions enables measuring the displacements over the entire axial range of a cell (>5 μm) with a 1-μm transverse resolution. Second, compared to digital holography and transmission-based phase imaging techniques, OCM rejects multiply scattered light and enables imaging highly scattering samples such as neural clusters and tissue (Badon et al., 2017). Third, angular modulation ensures that the system has no moving parts and the phase can be resolved in a single-shot ensuring better phase stability, although this configuration induces more speckle in the image compared to on-axis spatially-incoherent full-field OCM (Xiao et al., 2016). Moreover, the quality of the complex-valued images from off-axis OCM can be improved using computational adaptive optics (Liu et al., 2017; Rodríguez and Ji, 2018) for correcting both geometric (STAR Methods) and wavefront aberrations (Sudkamp et al., 2018).

SPoOF OCM could obtain the changes to birefringence by observing the retardation angle over the entire FOV. Previous studies have reported displacements from neuronal activity anywhere between 0.5 and 10 nm (Akkin et al., 2009; Hu et al., 2019; Ling et al., 2018; Yang et al., 2018). The phase sensitivity of SPoOF OCM while imaging a flat mirror was estimated to be 300 pm for each polarization state. On one hand, using a camera with a high full-well capacity is also critical to improving the phase stability of SPoOF OCM. On the other hand, to image at 4,000 Hz, the exposure times used were very low which may not effectively utilize the full-well capacity of the camera (Hosseini et al., 2016). Because all pixels in the two polarization states are detected simultaneously, the common noise from each pixel is removed by finding common phase fluctuations across all pixels. Alternatively, the phase stability could be improved by implementing temporal averaging algorithms. Using a faster camera would enable averaging more frames to improve the signal-to-noise ratios of phase responses (Shemonski et al., 2014). There are faster cameras available that can image up to 20,000 Hz at the same resolution from the same manufacturer (Photron USA Inc., San Diego, CA) and even for 75,000 Hz from other manufacturers (Phantom, Vision Research Inc., Wayne, NJ, and Specialised Imaging Ltd., Pitstone, United Kingdom). A few of these products also enable continuous memory streaming over the CXP protocols, which is considerably faster than streaming over ethernet. However, as the frame rate increases, the exposure time needs to be decreased further, which would demand higher incident optical power. Improving the phase stability is also critical to expanding SPoOF OCM for *in vivo* applications. Although the intrinsic axial sectioning capability of OCM makes it optimal for imaging highly scattering tissue samples, the phase stability of live samples is expected to be significantly lower compared to the *in vitro* samples demonstrated in this manuscript. For instance, Jonnal et al. (2012) determined that their phase stability ranged from 1.1 to 1.8 rad before filtering for retinal imaging. Besides improving the stability of the system with the aforementioned techniques, computational algorithms such as phase registering (Shemonski et al., 2014, 2015), averaging, and filtering (Hillmann et al., 2016) were previously used to improve the phase sensitivity of the OCM and OCT systems for dynamic functional imaging.

Several mechanisms have been thought to be behind the optical changes associated with neuronal activity. Because the electrical activity of the neurons does not happen in isolation, a part of the measured responses arises from intrinsic thermal/mechanical perturbations, physiological movements of proteins and sub-cellular compartments, and artifacts uncorrelated with the electrical activity. However, the validation with TTX treatment establishes the role of Na^+ channels in the measured optical responses from SPoOF OCM. The spike responses that were observed using the phase changes have been attributed to variations in the optical path length because of changes in the refractive index from ion flux (Berlind et al., 2008; Oh et al., 2012) and local swelling of the cell membrane (Kim et al., 2007; Yang et al., 2018). In this paper, we presented several measurements from SPoOF OCM images that utilized the changes to the magnitude and phase of the two polarization states in various ways. First, the cumulative phase response was devised to encode both phase and birefringence changes. Second, the instantaneous SD of the cumulative phase response was established as a metric for the electrical activity of the neurons. Third, the mean and variance of the activity metric were used to represent the electrical activity over a longer time window. These demonstrations highlighted the optical characteristics of millisecond-scale neural activity which could be used to generate instantaneous correlation matrices and compare with electrophysiology responses qualitatively. The experimental schemes of these studies, the analysis of the correlation matrices, and the visualizations were chosen to emulate previous demonstrations of neurophysiology setups and studies (Berdondini et al., 2009; Pastore et al., 2018; Renteria et al., 2020; Voleti et al., 2019). These studies have analyzed their data either for specific ROIs (Renteria et al., 2020; Voleti et al., 2019), similar to the results shown in Figures 2, 3, and 4, or for the whole FOV at once (Pastore et al., 2018), similar to the results in Figures 5 and 6. Each of these experiments merits focused studies of its own to effectively utilize the spatiotemporal throughput of optophysiology with SPoOF OCM. For instance, the time-varying correlation matrices were used to describe statistical similarities between different ROIs in the current set of experiments; these similarities were used to infer connectivity patterns. Such analogies have been proven valid for both electrode-based (Berdondini et al., 2009; Pastore et al., 2018) and optical neurophysiology setups (Renteria et al., 2020; Voleti et al., 2019). However, the origin of these connectivity patterns, be it mechanical, electrical, synaptical, or chemical, could be discerned using physical or pharmacological modulation of the cultured neural network, which could provide further context to the interpretability of these results for specific biological systems. It could further be expanded to utilize matrix factorization techniques to automatically identify the regions in the sample with correlated fluctuations that are specific to the electrical activity.

A key step to achieving this goal is to translate the optical measurements of optical path length and birefringence changes into electrical ones. However, OCM only measures changes to the optical path length

along the direction of beam propagation; quantifying these displacement patterns to potential differences and current flow requires prior knowledge of the cell density, orientation, and composition. For instance, the shape of the cell, the dry mass, the local cytoskeletal structure, and the presence of myelin sheath can each affect the phase and polarization-sensitive measurements (Eugui et al., 2018; Wang et al., 2016) of SPoOF OCM. Although we have demonstrated that each millisecond-scale spike observed by the electrical measurements had optical counterparts for the spontaneous activity of mammalian neurons, deriving the electrical potentials from the optical changes needs more accurate quantification of the birefringence. Our attempt at quantifying the birefringence of SPoOF OCM had a lower sensitivity compared to the cumulative phase responses (see Figure S3) and the calibration of the birefringence with a quarter-wave plate for experimental evaluation of the Jones matrix was negatively affected by the objective lens and the polarization noise of our light source. In addition, we hypothesized that the spiking activity was because of both Na^+ and K^+ ion channels; each channel could have its unique phase and polarization signatures. Therefore, observing the optical responses of each channel separately could further improve the accuracy of quantifying optical responses to electrical measurements. These measurements would also enable constructing the distinctive pulse profiles of the optical responses corresponding to action and postsynaptic potentials.

Compared to electrical measurements that usually measure the cumulative electrical changes of a whole cell, SPoOF OCM measures optical changes on a subcellular scale. For instance, the activity at 612.5 to 625 ms localized to a single cell at ξ_2 in Figure 5 was determined by observing several pixels that displayed an increase to the instantaneous SD of the phase changes in a 12.5 ms temporal window. Therefore, the first step toward converting the optical changes to membrane potentials will involve developing methods to normalize and cumulate individual pixel-level changes (Savtchenko et al., 2017). In addition, the electrode placed near the cell has nanometer-scale vibrations as a result of minute instabilities in mounting; therefore, the cell that is directly in contact with the electrode has larger phase noise compared to cells away from the electrode. Comparing the optical changes from just that cell with the electrode measurements is challenging. Hence, we used field-potential measurements to collect the neural activity from a larger region in the sample that is less affected by the electrode motion and compared the cumulative responses of ROIs close to the electrode tip. Alternatively, previous studies overcame this issue by culturing cells on multielectrode arrays (Ling et al., 2018). Moreover, SPoOF OCM measures changes to the optical path length or the birefringence along the direction of propagation of light. The orientation of the ion channels along the cellular structures could drastically affect SPoOF OCM measurements. In future studies, the polarization-sensitive measurements of SPoOF OCM will be quantified to measure the birefringence and cellular orientation; the phase changes can be projected along the cellular orientation to normalize the responses from different cells. In addition, because spatial compartmentalization of ion flux could limit our ability to convert pixel-level changes to cumulative cellular activity; future studies will concentrate on trying to isolate the responses from the different voltage-dependent ion channels by selectively blocking them one by one. In this study, TTX was used to block Na^+ channels; we plan to extend this to treatment with 4-aminopyridine for voltage-gated K^+ channels (Solari et al., 2002) and blockers such as ziconotide for N-type Ca^{2+} channels (McGivern, 2007) in future experiments. The optical characteristics of each channel could be individually profiled and cumulated to convert optical responses into electrophysiological measurements. Recent studies have precisely calibrated the relationship between the incident optical power on optically-sensitive neurons and the number of action potentials evoked in response (Sridharan et al., 2022). A similar experimental strategy could be adapted to observe the optical response profiles of optically-triggered individual action potentials, without the need for electrodes that reduce the phase stability of the measurements. Finally, although the goal of SPoOF OCM was to improve the throughput of traditional electrophysiology techniques, the dataset is overwhelmingly large to process and visualize all at once. Therefore, to highlight the utility of SPoOF OCM, the results demonstrated in the paper were conducted for several ROIs. Although image reconstruction was performed on a graphics processing unit (GPU), future studies will explore utilizing the complete spatiotemporal throughput for deriving further insights into neural activity by matching the ultra-parallel acquisition with ultra-parallel processing on a GPU completely. In addition, dimensionality reduction algorithms could be used to extract the information from SPoOF OCM responses more effectively. Prevalent techniques for dimensionality reduction in neurophysiology are principal component analysis and k-means clustering (Dombeck et al., 2009; Pang et al., 2016). A representative implementation of these techniques for the data in Figure 5 is described in and the results are shown in Figure S8; future studies will utilize these techniques for both calibration of the optical responses to electrical ones and extraction of connectivity patterns in the overall network.

In conclusion, SPoOF OCM can achieve label-free full-field imaging at a millisecond timescale and with a micron spatial scale over several seconds and over hundreds of microns by tracking both phase-sensitive and polarization-sensitive changes associated with neural activity. We believe that SPoOF OCM provides a multimodal setup for transitioning from electrophysiological techniques to next-gen optophysiological techniques.

Limitations of the study

Because the neural activity in SPoOF OCM typically causes optical path length changes of a few nanometers, the current study was conducted on *in vitro* models to maintain the phase stability of the imaging system to meet these limits. In the future, computational phase stability correction using guide-star-based or common-mode noise rejection algorithms can help translate this technique to *in vivo* imaging.

The current study was not able to quantify the optical activity patterns into the electrical metrics such as voltage or current that are typically used in electrophysiology. Techniques to achieve this in future studies have been described in the paper.

Because angular modulation of the reference requires the excitation source to have relatively high spatial coherence, the intensity images contained a lot of speckles. Future upgrades to the system will involve tuning the spatial coherence to balance the modulation efficiency and speckle reduction.

STAR★METHODS

Detailed methods are provided in the online version of this paper and include the following:

- KEY RESOURCES TABLE
- RESOURCE AVAILABILITY
  - Lead contact
  - Materials availability
  - Data and code availability
- EXPERIMENTAL MODEL AND SUBJECT DETAILS
  - Cell culture
- METHOD DETAILS
  - SPoOF OCM system setup
  - Image reconstruction
  - Signal processing
  - Electrical stimulation and electrophysiology
- QUANTIFICATION AND STATISTICAL ANALYSIS

SUPPLEMENTAL INFORMATION

Supplemental information can be found online at https://doi.org/10.1016/j.isci.2022.104307.

AUTHOR CONTRIBUTIONS

Conceptualization, Y-Z.L., R.R.I., and S.A.B.; Software, Formal analysis, Visualization, and Investigation, R.R.I.; Resources: R.R.I., Y-Z.L., C.A.R., and B.E.T.; Methodology, R.R.I., C.A.R., H.C., and M.Z.; Writing, R.R.I., Y-Z.L., and S.A.B.; Supervision and Funding Acquisition, S.A.B.

DECLARATION OF INTERESTS

The authors declare no competing interests.

REFERENCES

Akkin, T., Joo, C., and de Boer, J.F. (2007). Depth-resolved measurement of transient structural changes during action potential propagation. Biophys. J. *93*, 1347–1353. https://doi.org/10.1529/biophysj.106.091298.

Akkin, T., Landowne, D., and Sivaprakasam, A. (2010). Detection of neural action potentials using optical coherence tomography: intensity and phase measurements with and without dyes. Front. Neurogenet. *2*, 22. https://doi.org/10.3389/fnene.2010.00022.

Akkin, T., Landowne, D., and Sivaprakasam, A. (2009). Optical coherence tomography phase measurement of transient changes in squid giant axons during activity. J. Membr. Biol. *231*, 35–46. https://doi.org/10.1007/s00232-009-9202-4.

Anděrová, M., Kubinová, Š., Jelitai, M., Neprašová, H., Glogarová, K., Prajerová, I., Urdzíková, L., Chvátal, A., and Syková, E. (2006). Transplantation of embryonic neuroectodermal progenitor cells into the site of a photochemical lesion: immunohistochemical and electrophysiological analysis. J. Neurobiol. *66*, 1084–1100. https://doi.org/10.1002/neu.20278.

Auksorius, E., and Boccara, A.C. (2020). High-throughput dark-field full-field optical coherence tomography. Opt. Lett. *45*, 455. https://doi.org/10.1364/OL.381888.

Badon, A., Boccara, A.C., Lerosey, G., Fink, M., and Aubry, A. (2017). Multiple scattering limit in optical microscopy. Opt. Express *25*, 28914. https://doi.org/10.1364/OE.25.028914.

Badreddine, A.H., Jordan, T., and Bigio, I.J. (2016). Real-time imaging of action potentials in nerves using changes in birefringence. Biomed. Opt. Express *7*, 1966. https://doi.org/10.1364/BOE.7.001966.

Baran, U., and Wang, R.K. (2016). Review of optical coherence tomography based angiography in neuroscience. Neurophotonics *3*, 10902. https://doi.org/10.1117/1.NPh.3.1.010902.

Batabyal, S., Satpathy, S., Bui, L., Kim, Y.-T., Mohanty, S., Bachoo, R., and Davé, D.P. (2017). Label-free optical detection of action potential in mammalian neurons. Biomed. Opt. Express *8*, 3700. https://doi.org/10.1364/BOE.8.003700.

Berdondini, L., Imfeld, K., Maccione, A., Tedesco, M., Neukom, S., Koudelka-Hep, M., and Martinoia, S. (2009). Active pixel sensor array for high spatio-temporal resolution electrophysiological recordings from single cell to large scale neuronal networks. Lab. Chip *9*, 2644. https://doi.org/10.1039/b907394a.

Berlind, T., Pribil, G.K., Thompson, D., Woollam, J.A., and Arwin, H. (2008). Effects of ion concentration on refractive indices of fluids measured by the minimum deviation technique. Phys. Status Solidi C *5*, 1249–1252. https://doi.org/10.1002/pssc.200777897.

Carter, K.M., George, J.S., and Rector, D.M. (2004). Simultaneous birefringence and scattered light measurements reveal anatomical features in isolated crustacean nerve. J. Neurosci. Methods *135*, 9–16. https://doi.org/10.1016/j.jneumeth.2003.11.010.

Carter, M., and Shieh, J. (2015). Visualizing neural function. In Guide to Research Techniques in Neuroscience (Elsevier), pp. 167–183.

Chen, Y., Aguirre, A.D., Ruvinskaya, L., Devor, A., Boas, D.A., and Fujimoto, J.G. (2009). Optical coherence tomography (OCT) reveals depth-resolved dynamics during functional brain activation. J. Neurosci. Methods *178*, 162–173. https://doi.org/10.1016/j.jneumeth.2008.11.026.

Collot, M., Ashokkumar, P., Anton, H., Boutant, E., Faklaris, O., Galli, T., Mély, Y., Danglot, L., and Klymchenko, A.S. (2019). MemBright: a family of fluorescent membrane probes for advanced cellular imaging and neuroscience. Cell Chem. Biol. *26*, 600–614.e7. https://doi.org/10.1016/j.chembiol.2019.01.009.

Dombeck, D.A., Graziano, M.S., and Tank, D.W. (2009). Functional clustering of neurons in motor cortex determined by cellular resolution imaging in awake behaving mice. J. Neurosci. Off. J. Soc. Neurosci. *29*, 13751–13760. https://doi.org/10.1523/JNEUROSCI.2985-09.2009.

Eugui, P., Lichtenegger, A., Augustin, M., Harper, D.J., Muck, M., Roetzer, T., Wartak, A., Konegger, T., Widhalm, G., Hitzenberger, C.K., et al. (2018). Beyond backscattering: optical neuroimaging by BRAD. Biomed. Opt. Express *9*, 2476. https://doi.org/10.1364/BOE.9.002476.

Foust, A.J., and Rector, D.M. (2007). Optically teasing apart neural swelling and depolarization. Neuroscience *145*, 887–899. https://doi.org/10.1016/j.neuroscience.2006.12.068.

Graf, B.W., Ralston, T.S., Ko, H.-J., and Boppart, S.A. (2009). Detecting intrinsic scattering changes correlated to neuron action potentials using optical coherence imaging. Opt. Express *17*, 13447. https://doi.org/10.1364/OE.17.013447.

Hill, B.C., Schubert, E.D., Nokes, M.A., and Michelson, R.P. (1977). Laser interferometer measurement of changes in crayfish axon diameter concurrent with action potential. Science *196*, 426–428. https://doi.org/10.1126/science.850785.

Hillmann, D., Spahr, H., Pfäffle, C., Sudkamp, H., Franke, G., and Hüttmann, G. (2016). *In vivo* optical imaging of physiological responses to photostimulation in human photoreceptors. Proc. Natl. Acad. Sci. *113*, 13138–13143. https://doi.org/10.1073/pnas.1606428113.

Hosseini, P., Zhou, R., Kim, Y.-H., Peres, C., Diaspro, A., Kuang, C., Yaqoob, Z., and So, P.T.C. (2016). Pushing phase and amplitude sensitivity limits in interferometric microscopy. Opt. Lett. *41*, 1656. https://doi.org/10.1364/OL.41.001656.

Hu, C., Sam, R., Shan, M., Nastasa, V., Wang, M., Kim, T., Gillette, M., Sengupta, P., and Popescu, G. (2019). Optical excitation and detection of neuronal activity. J. Biophotonics *12*, e201800269. https://doi.org/10.1002/jbio.201800269.

Jelitai, M., Anderová, M., Chvátal, A., and Madarász, E. (2007). Electrophysiological characterization of neural stem/progenitor cells during *in vitro* differentiation: study with an immortalized neuroectodermal cell line. J. Neurosci. Res. *85*, 1606–1617. https://doi.org/10.1002/jnr.21282.

Ji, N., Freeman, J., and Smith, S.L. (2016). Technologies for imaging neural activity in large volumes. Nat. Neurosci. *19*, 1154–1164. https://doi.org/10.1038/nn.4358.

Jonnal, R.S., Kocaoglu, O.P., Wang, Q., Lee, S., and Miller, D.T. (2012). Phase-sensitive imaging of the outer retina using optical coherence tomography and adaptive optics. Biomed. Opt. Express *3*, 104. https://doi.org/10.1364/BOE.3.000104.

Kim, G.H., Kosterin, P., Obaid, A.L., and Salzberg, B.M. (2007). A mechanical spike accompanies the action potential in mammalian nerve terminals. Biophys. J. *92*, 3122–3129. https://doi.org/10.1529/biophysj.106.103754.

Koike-Tani, M., Tominaga, T., Oldenbourg, R., and Tani, T. (2019). Instantaneous polarized light imaging reveals activity dependent structural changes of dendrites in mouse hippocampal slices. Preprint at bioRxiv. https://doi.org/10.1101/523571.

Larivière-Loiselle, C., Bélanger, E., and Marquet, P. (2020). Polychromatic digital holographic microscopy: a quasicoherent-noise-free imaging technique to explore the connectivity of living neuronal networks. Neurophotonics *7*, 40501. https://doi.org/10.1117/1.NPh.7.4.040501.

Lazebnik, M., Marks, D.L., Potgieter, K., Gillette, R., and Boppart, S.A. (2003). Functional optical coherence tomography for detecting neural activity through scattering changes. Opt. Lett. *28*, 1218. https://doi.org/10.1364/OL.28.001218.

Lecoq, J., Orlova, N., and Grewe, B.F. (2019). Wide. Fast. Deep: recent advances in multiphoton microscopy of *in vivo* neuronal activity. J. Neurosci. *39*, 9042–9052. https://doi.org/10.1523/JNEUROSCI.1527-18.2019.

Li, X., Krol, M.A., Jahani, S., Boas, D.A., Tager-Flusberg, H., and Yücel, M.A. (2020). Brain correlates of motor complexity during observed and executed actions. Sci. Rep. *10*, 10965. https://doi.org/10.1038/s41598-020-67327-5.

Ling, T., Boyle, K.C., Goetz, G., Zhou, P., Quan, Y., Alfonso, F.S., Huang, T.W., and Palanker, D. (2018). Full-field interferometric imaging of propagating action potentials. Light Sci. Appl. *7*, 107. https://doi.org/10.1038/s41377-018-0107-9.

Liu, Y.-Z., South, F.A., Xu, Y., Carney, P.S., and Boppart, S.A. (2017). Computational optical coherence tomography [Invited]. Biomed. Opt. Express *8*, 1549. https://doi.org/10.1364/BOE.8.001549.

Lu, R.-W., Zhang, Q.-X., and Yao, X.-C. (2011). Circular polarization intrinsic optical signal recording of stimulus-evoked neural activity. Opt. Lett. *36*, 1866. https://doi.org/10.1364/OL.36.001866.

Marquet, P., Depeursinge, C., and Magistretti, P.J. (2014). Review of quantitative phase-digital holographic microscopy: promising novel imaging technique to resolve neuronal network activity and identify cellular biomarkers of psychiatric disorders. Neurophotonics *1*, 20901. https://doi.org/10.1117/1.NPh.1.2.020901.

McGivern, J.G. (2007). Ziconotide: a review of its pharmacology and use in the treatment of pain. Neuropsychiatr. Dis. Treat. *3*, 69–85. https://doi.org/10.2147/nedt.2007.3.1.69.

Oh, S., Fang-Yen, C., Choi, W., Yaqoob, Z., Fu, D., Park, Y., Dassari, R.R., and Feld, M.S. (2012). Label-free imaging of membrane potential using membrane electromotility. Biophys. J. *103*, 11–18. https://doi.org/10.1016/j.bpj.2012.05.020.

Pang, R., Lansdell, B.J., and Fairhall, A.L. (2016). Dimensionality reduction in neuroscience. Curr. Biol. *26*, R656–R660. https://doi.org/10.1016/j.cub.2016.05.029.

Pastore, V.P., Massobrio, P., Godjoski, A., and Martinoia, S. (2018). Identification of excitatory-inhibitory links and network topology in large-scale neuronal assemblies from multi-electrode recordings. PLoS Comput. Biol. *14*, e1006381. https://doi.org/10.1371/journal.pcbi.1006381.

Renteria, C., Liu, Y.-Z., Chaney, E.J., Barkalifa, R., Sengupta, P., and Boppart, S.A. (2020). Dynamic tracking algorithm for time-varying neuronal network connectivity using wide-field optical image video sequences. Sci. Rep. *10*, 2540. https://doi.org/10.1038/s41598-020-59227-5.

Rodríguez, C., and Ji, N. (2018). Adaptive optical microscopy for neurobiology. Curr. Opin. Neurobiol. *50*, 83–91. https://doi.org/10.1016/j.conb.2018.01.011.

Savtchenko, L.P., Poo, M.M., and Rusakov, D.A. (2017). Electrodiffusion phenomena in neuroscience: a neglected companion. Nat. Rev. Neurosci. *18*, 598–612. https://doi.org/10.1038/nrn.2017.101.

Schlett, K., and Madarász, E. (1997). Retinoic acid induced neural differentiation in a neuroectodermal cell line immortalized by p53 deficiency. J. Neurosci. Res. *47*, 405–415. https://doi.org/10.1002/(sici)1097-4547(19970215)47:4<405::aid-jnr6>3.0.co;2-i.

Shemonski, N.D., Adie, S.G., Liu, Y.-Z., South, F.A., Carney, P.S., and Boppart, S.A. (2014). Stability in computed optical interferometric tomography (Part I): stability requirements. Opt. Express *22*, 19183. https://doi.org/10.1364/OE.22.019183.

Shemonski, N.D., South, F.A., Liu, Y.-Z., Adie, S.G., Scott Carney, P., and Boppart, S.A. (2015). Computational high-resolution optical imaging of the living human retina. Nat. Photonics *9*, 440–443. https://doi.org/10.1038/nphoton.2015.102.

Solari, A., Uitdehaag, B.M., Giuliani, G., Pucci, E., and Taus, C. (2002). Aminopyridines for symptomatic treatment in multiple sclerosis. Cochrane Database Syst. Rev.Cd001330 https://doi.org/10.1002/14651858.CD001330.

Son, T., Wang, B., Thapa, D., Lu, Y., Chen, Y., Cao, D., and Yao, X. (2016). Optical coherence tomography angiography of stimulus evoked hemodynamic responses in individual retinal layers. Biomed. Opt. Express *7*, 3151. https://doi.org/10.1364/BOE.7.003151.

Sridharan, S., Gajowa, M.A., Ogando, M.B., Jagadisan, U.K., Abdeladim, L., Sadahiro, M., Bounds, H.A., Hendricks, W.D., Turney, T.S., Tayler, I., et al. (2022). High-performance microbial opsins for spatially and temporally precise perturbations of large neuronal networks. Neuron *110*, 1139–1155.e6. https://doi.org/10.1016/j.neuron.2022.01.008.

Stepnoski, R.A., LaPorta, A., Raccuia-Behling, F., Blonder, G.E., Slusher, R.E., and Kleinfeld, D. (1991). Noninvasive detection of changes in membrane potential in cultured neurons by light scattering. Proc. Natl. Acad. Sci. *88*, 9382–9386. https://doi.org/10.1073/pnas.88.21.9382.

Stosiek, C., Garaschuk, O., Holthoff, K., and Konnerth, A. (2003). *In vivo* two-photon calcium imaging of neuronal networks. Proc. Natl. Acad. Sci. *100*, 7319–7324. https://doi.org/10.1073/pnas.1232232100.

Strangman, G., Boas, D.A., and Sutton, J.P. (2002). Non-invasive neuroimaging using near-infrared light. Biol. Psychiatry *52*, 679–693. https://doi.org/10.1016/S0006-3223(02)01550-0.

Sudkamp, H., Hillmann, D., Koch, P., Vom Endt, M., Spahr, H., Münst, M., Pfäffle, C., Birngruber, R., and Hüttmann, G. (2018). Simple approach for aberration-corrected OCT imaging of the human retina. Opt. Lett. *43*, 4224. https://doi.org/10.1364/OL.43.004224.

Sudkamp, H., Koch, P., Spahr, H., Hillmann, D., Franke, G., Münst, M., Reinholz, F., Birngruber, R., and Hüttmann, G. (2016). *In-vivo* retinal imaging with off-axis full-field time-domain optical coherence tomography. Opt. Lett. *41*, 4987. https://doi.org/10.1364/OL.41.004987.

Varga, B.V., Hádinger, N., Gócza, E., Dulberg, V., Demeter, K., Madarász, E., and Herberth, B. (2008). Generation of diverse neuronal subtypes in cloned populations of stem-like cells. BMC Dev. Biol. *8*, 89. https://doi.org/10.1186/1471-213X-8-89.

Voleti, V., Patel, K.B., Li, W., Perez Campos, C., Bharadwaj, S., Yu, H., Ford, C., Casper, M.J., Yan, R.W., Liang, W., et al. (2019). Real-time volumetric microscopy of *in vivo* dynamics and large-scale samples with SCAPE 2.0. Nat. Methods *16*, 1054–1062. https://doi.org/10.1038/s41592-019-0579-4.

Wang, H., Akkin, T., Magnain, C., Wang, R., Dubb, J., Kostis, W.J., Yaseen, M.A., Cramer, A., Sakadžić, S., and Boas, D. (2016). Polarization sensitive optical coherence microscopy for brain imaging. Opt. Lett. *41*, 2213. https://doi.org/10.1364/OL.41.002213.

Wu, J., Liang, Y., Chen, S., Hsu, C.-L., Chavarha, M., Evans, S.W., Shi, D., Lin, M.Z., Tsia, K.K., and Ji, N. (2020). Kilohertz two-photon fluorescence microscopy imaging of neural activity *in vivo*. Nat. Methods *17*, 287–290. https://doi.org/10.1038/s41592-020-0762-7.

Xiao, P., Fink, M., and Boccara, A.C. (2016). Full-field spatially incoherent illumination interferometry: a spatial resolution almost insensitive to aberrations. Opt. Lett. *41*, 3920. https://doi.org/10.1364/OL.41.003920.

Yang, Y., Liu, X.-W., Wang, H., Yu, H., Guan, Y., Wang, S., and Tao, N. (2018). Imaging action potential in single mammalian neurons by tracking the accompanying sub-nanometer mechanical motion. ACS Nano *12*, 4186–4193. https://doi.org/10.1021/acsnano.8b00867.

Yeh, Y.-J., Black, A.J., Landowne, D., and Akkin, T. (2015). Optical coherence tomography for cross-sectional imaging of neural activity. Neurophotonics *2*, 1. https://doi.org/10.1117/1.NPh.2.3.035001.

Yost, S.C. (1999). Potassium Channels. Anesthesiology *90*, 1186–1203. https://doi.org/10.1097/00000542-199904000-00035.

Zhang, Y., Yao, L., Yang, F., Yang, S., Edathodathil, A., Xi, W., Roe, A.W., and Li, P. (2020). INS-fOCT: a label-free, all-optical method for simultaneously manipulating and mapping brain function. Neurophotonics *7*, 1. https://doi.org/10.1117/1.NPh.7.1.015014.

STAR★METHODS

KEY RESOURCES TABLE

REAGENT or RESOURCE	SOURCE	IDENTIFIER
Chemicals, peptides, and recombinant proteins		
Eagle's modified essential medium	Corning, Corning NY, USA	10009CV
Fetal bovine serum	Thermo Fisher Scientific, Waltham MA, USA	16140071
1% v/v Penicillin-Streptomycin	Thermo Fisher Scientific, Waltham MA, USA	10378016
All-trans Retinoic acid	Fisher Scientific, Waltham MA, USA	MP021902696
Tetrodotoxin	Biotium Fremont CA, USA	00060
Citric acid	Fisher Scientific, Waltham MA, USA	A940-500
Sodium citrate	Fisher Scientific, Waltham MA, USA	S279-500
Experimental models: Cell lines		
NE-4C mouse neuroectodermal cells	American Type Culture Collection, Manassas VA, USA	CRL-2925; RRID:CVCL_B063
Software and algorithms		
MATLAB	Mathworks Inc.	2019b
LabVIEW	National Instruments	2019
CUDA Toolkit	NVIDIA Corp.	10.1
Visual Studio	Microsoft	Community 2019
Other		
Super luminescent diode	Superlum Inc., Cork, Ireland	S860-HP
Objective lens(es)	Olympus Inc.	UMPLanFL-N, 20x, 0.50 W
Camera	Photron, Tokyo, Japan	Mini AX 100
Data acquisition card	National Instruments	DAQ PCIe-6353
Micropipette electrode	AM systems	573050 suction electrodes
Neuroamplifier	AM systems	Model 1700
Analog stimulus isolator	AM systems	Model 2200

RESOURCE AVAILABILITY

Lead contact

Further information and requests for resources and reagents should be directed to and will be fulfilled by the lead contact, Stephen A. Boppart (boppart@illinois.edu).

Materials availability

This study did not generate new unique reagents.

Data and code availability

All data reported in this paper will be shared by the lead contact upon request and through a collaborative research agreement since the raw data are too large to be uploaded to public repositories.

All original code used to analyze and process the results in the paper are available at https://doi.org/10.5281/zenodo.6450456.

Any additional information required to reanalyze the data reported in this paper is available from the lead contact upon request.

EXPERIMENTAL MODEL AND SUBJECT DETAILS

Cell culture

Secondary cultures of NE-4C mouse neuroectodermal cells (CRL-2925, American Type Culture Collection, Manassas, VA, USA | RRID:CVCL_B063) were plated on a 35-mm glass-bottom Petri dish with a cell adherent coating and grown in Eagle's modified essential medium with a total of 4 μM L-glutamine (10009CV, Corning, Corning, NY, USA), supplemented with 10% v/v fetal bovine serum (16140071, Thermo Fisher Scientific, Waltham, MA, USA) and 1% v/v Penicillin-Streptomycin (10378016, Thermo Fisher Scientific) for 30 h in an incubator at 37°C in an environment with 95% air and 5% CO_2. A 1 μM solution of all-trans retinoic acid in DMSO was added to the dishes on day 2 (after plating) and the media was replaced every day for 5 additional days. The cells were grown and plated on poly-L-lysine coated surfaces. The cells were imaged at room temperature on day 7 within 30 min of being taken out of the incubator.

NE-4C cells have been established as an appropriate neuronal model where voltage-dependent currents (Schlett and Madarász, 1997; Varga et al., 2008), TTX-sensitive sodium currents, and K_{DR} currents were observed even early into the induction phase (day 2) (Jelitai et al., 2007). Brightfield and fluorescence images of NE-4C cells are shown in Figure S9 to show the typical morphologies of the cells used in these experiments. The cells were derived from 9-day-old mouse embryos of unknown sex lacking functional p53 genes (Schlett and Madarász, 1997). TTX solution was prepared by dissolving 1 mg of the power in 1 mL citrate buffer (pH 4.8; prepared by mixing 4 mL 0.1 M citric acid and 6 mL 0.1 M Trisodium citrate). For a final TTX concentration of 100 nM, 1 μL of this solution was further dissolved in 31 mL of media , which was then added to the cells. Cell media without TTX was used as control. The cells were incubated with TTX (or control) for at least 20 min in the incubator before imaging. For Figure S7, the cell culture dish was marked with respect to the sample holder for orientation to find the same field-of-view after incubation with TTX.

For the fluorescence images in Figure S9, Fluo-4 (F14201, ThermoFisher Scientific, Waltham MA, USA) in DMSO was added to the cells at 1 μM. The cells were incubated at 37°C for 30 min. The media was the replaced and the cells were incubated for another hour. Finally, imaging was performed with a custom widefield fluorescence microscope in reflectance mode at 10 Hz with at 20x magnification.

METHOD DETAILS

SPoOF OCM system setup

SPoOF OCM was designed to generate two *en face* complex-valued OCM images at two different polarization states. As seen in Figure 1A, a partially polarized superluminescent diode centered at 860 nm (S860-HP, Superlum Inc., Cork, Ireland) sources a Mack-Zehnder interferometer where the sample and the reference arms use the same objective lens (UMPLanFL-N, 20x, 0.50 NA, Olympus Inc.) to match dispersion. The light incident on the sample arm objective was circularly polarized. The reference arm contains two separate custom gratings (Thorlabs Inc., Newton NJ) to spatially modulate each polarization state in orthogonal directions while maintaining a large field-of-view while minimizing the effects of tilt arising from the off-axis reference beams. The zero-order reflections from both gratings were aligned in the far-field and to the far-field of the backscattered light from the sample plane. The optical path lengths of both polarization states were matched by minimizing the difference between the phase of the scattered field from a flat mirror when the intensity was maximized. After alignment, the zero-order and higher-order beams of the reference arms were blocked using a spatial band-pass filter. The detector comprises a 12-bit camera with a full-well capacity of 16,000 e⁻ capable of imaging at 4,000 fps for the full FOV (Mini AX100, Photron, Tokyo, Japan). An optional high-pass filter could be inserted into the imaging setup between L_4 and L_5 to enable dark-field imaging (Auksorius and Boccara, 2020).

Image reconstruction

All steps for image reconstruction and processing are shown in Figure S2. Image reconstruction for SPoOF OCM, as seen in Figure 1B, involved spatially demodulating the complex-valued Fourier image of each frame to obtain a 400 × 400-pixel^2 reconstructed image spanning 200 × 200 μm^2. However, vignetting effects reduce the FOV to a circular aperture with a diameter of 200 μm.

First, the images from the camera were reconstructed on a graphical processing unit (GPU) described by Equation (4).

$$\tilde{I}_{Camera}(k_x, k_y) = \mathcal{F}_{x \to k_x, y \to k_y}\{I_{Camera}(x, y)\},$$

$$E_{P1}^{Recon}(x, y) = \mathcal{F}^{-1}_{k_x - k_x^{P1} \to x, k_y - k_y^{P1} \to y}\left\{\tilde{I}_{Camera}\left(k_x - k_x^{P1}, k_y - k_y^{P1}\right) \times W\left(k_x - k_x^{P1}, k_y - k_y^{P1}\right)\right\}, \text{ and}$$

$$E_{P2}^{Recon}(x, y) = \mathcal{F}^{-1}_{k_x - k_x^{P2} \to x, k_y - k_y^{P2} \to y}\left\{\tilde{I}_{Camera}\left(k_x - k_x^{P2}, k_y - k_y^{P2}\right) \times W\left(k_x - k_x^{P2}, k_y - k_y^{P2}\right)\right\},$$

(Equation 4)

where I_{Camera} is the raw image from the camera, and $\tilde{I}_{Camera}$ is the two-dimensional (2D) spatial Fourier transform of I_{Camera}. As seen in Figure 1, SPoOF OCM raw images contain two separate spatial modulations encoding the complex-valued images at two different polarization states, P1 and P2. k_x^{P1} and k_y^{P1} represent the centers of the modulation for P1 in the 2D Fourier plane, and k_x^{P2} and k_y^{P2} for P2. The reconstructed images, E_{P1}^{Recon} and E_{P2}^{Recon}, are obtained through a 2D inverse Fourier transform centered at $(k_x - k_x^{P1}, k_y - k_y^{P1})$ and $(k_x - k_x^{P1}, k_y - k_y^{P1})$, respectively. W represents a circular 2D Tukey window in the 2D Fourier plane to "crop" the spatial modulation out of the polarization state from $\tilde{I}_{Camera}$.

For the setup presented in the paper, both I_{Camera} and $\tilde{I}_{Camera}$ consisted of 1024 × 1024 pixels. The grating pattern and the optics were chosen to ensure that the modulations were as far away as possible from the DC component of $\tilde{I}_{Camera}$ while still maintaining the sampling criteria. Since we wanted to cover a field of view with a diameter of 200 μm and a spatial resolution of approximately 1 μm, the reconstructed images must span 400 pixels in each direction. Therefore, the k_x^{P1}, k_y^{P1}, k_x^{P2}, and k_y^{P2} were all maintained to be approximately 200 pixels from the edge of $\tilde{I}_{Camera}$ and W was chosen to have a window size of 200 pixels and a tapering factor of 0.96. The aforementioned steps were performed on a GPU using the CUDA and CUFFT libraries (NVIDIA Corporation).

Due to the mismatch in the optical wavefront between the sample and reference arms, there was an additional phase flattening step required to obtain E_{P1} and E_{P2}. A phase mask, as described in Equation (5) is multiplied to each polarization state to obtain a "flat" phase profile.

$$E_{P1}(x, y) = E_{P1}^{Recon}(x, y)e^{j\left(\zeta_{x^2 P1}x^2 + \zeta_{y^2 P1}y^2 + \zeta_{x_{P1}}x + \zeta_{y_{P1}}y + \zeta_{xy_{P1}}xy + \zeta_{0_{P1}}\right)} \text{ and}$$

$$E_{P2}(x, y) = E_{P2}^{Recon}(x, y)e^{j\left(\zeta_{x^2 P2}x^2 + \zeta_{y^2 P2}y^2 + \zeta_{x_{P2}}x + \zeta_{y_{P2}}y + \zeta_{xy_{P2}}xy + \zeta_{0_{P2}}\right)},$$

(Equation 5)

where ζ_k are the real-valued polynomial coefficients which were manually tuned based on the profile of a flat surface for calibration. The coefficients were tuned to minimize the standard deviation of a phase in the circular aperture while imaging the surface of a flat mirror. Phase-flattening was mainly used to improve visualization and to avoid wrapping artifacts during spatial binning. E_{P1}^{Recon} and E_{P2}^{Recon} are the complex-valued demodulated images before phase flattering, and E_{P1} and E_{P2} are the images after demodulation shown illustrated in Figure 1B. While a phase difference of π/2 is expected between the two polarization states, the phase unwrapping digitally registers the phase of the two states during optimization and for ease of visualization. Therefore, the phase of E_{P2} is later shifted by π/2 during the estimation of the retardation angle. The spatial resolutions of the system were evaluated by imaging a high-resolution USAF target to determine the transverse resolution (Figure S10) and by moving the reference arm to different locations to determine the axial resolution, as seen in Figure 1C. The transverse and axial resolutions were measured to be 1 μm and 4.6 ± 0.1 μm respectively. The standard deviation of the phase over 2 s of either polarization state of a flat surface was estimated to be 600 pm before any filtering and 300 pm after filtering (See Figure S1 for details).

Data for SPoOF OCM was acquired using custom LabVIEW software (National Instruments) (Figure S11). The real-time display is operated at 25 fps and can operate indefinitely. However, at 4,000 fps, the camera streams 10,900 frames acquired within 2.5 s over ethernet for 7 min. The code for streaming data from the camera was written in C and compiled as a DLL. Similarly, the code for real-time processing was written in C using CUDA libraries. For SPoOF OCM, the algorithm in Figure 1B was implemented on a GPU to generate demodulated SPoOF OCM images. The code reconstructs SPoOF OCM images at 50 frames per second, fast enough for real-time display, and takes 218 s for reconstructing the entire dataset.

Signal processing

The ROIs in Figure 2 were sorted based on their belonging to a cluster and their proximity to the electrode tip whereas, in Figures 4 and 5, the ROIs were sorted solely based on their proximity to the electrode tip. The complex-valued response of each ROI was spatially averaged. For a give ROI m and the polarization state P_n, the averaged response over a window w (= 2 for the results in this paper), $E_{ROI_m}^{P_n}(t)$, can be defined as

$$E_{ROI_m}^{P_n}(t) = \sum_{x=-w}^{w} \sum_{y=-w}^{w} E_{P1}\left(x + ROI_m^x, y + ROI_m^y, t\right). \quad \text{(Equation 6)}$$

For phase responses $\varphi_{ROI_m}^{P_n}(t)$, the mean phase of each ROI was iteratively shifted by multiplying the complex-valued response with a function of the form $e^{iq\psi}$ at iteration q until the difference between the maximum and minimum values of the phase in any 200 ms window was less than $\frac{\pi}{2}$.

$$\varphi_{ROI_m,q+1}^{P_n}(t) = \begin{cases} \angle\left(E_{ROI_m,q}^{P_n}(t)e^{iq\psi}\right), & \text{if } \max\varphi_{ROI_m,q}^{P_n}(t)\Big|_{t=s}^{s+200\ ms} - \min\varphi_{ROI_m,q}^{P_n}(t)\Big|_{t=s}^{s+200\ ms} \geq \frac{\pi}{2} \\ & \forall s \in \{0, 200, 400, ..., t_{max}\}\ ms \\ \angle\left(E_{ROI_m,q}^{P_n}(t)\right), & \text{otherwise} \end{cases}$$

(Equation 7)

This avoids any phase wrapping artifacts. The magnitude or the phase was filtered using a Gaussian filter defined as a Rational transfer function in time-domain with a window size of 8 and 3-dB cutoff at 2,000 Hz. In MATLAB (2019b, Mathworks Inc.), this was achieved using the `filter` function where the denominator coefficient was set to be 1. Next, the responses such as the retardation angle or the Euclidean distance of the phase responses from the two polarization states that were used to generate the results in the main manuscript were estimated from the Gaussian-filtered responses. We described the cumulative phase response as the Euclidian distance from the origin when the phases of the two detected OCM signals are assumed to form a Cartesian plane. An alternative derivation of this response can be obtained by neglecting the denominator, the arctangent function, and assuming the magnitudes of both states to be equal to 1, i.e. by neglecting the tree components of the retardation angle estimation that negatively affected the sensitivity. Since phase unwrapping digitally removes the π/2 phase difference between the two polarization states to estimate the optimal correction pattern, the phase of E_{P2} is additionally shifted by π/2 during estimation of the retardation angle. However, this shift was unnecessary for calculating the cumulative phase response. The temporal mean value of the response of each ROI was set to be zero by subtracting the low-frequency (<25 Hz) components of the signal. Finally, the mean response of the ROIs a long time was subtracted from each response to avoid any bulk motion artifacts or phase fluctuations due to thermal drifts. The derivation of these responses corresponds to the cyan sections in Figure S2 and was further used to obtain the results in the orange section and shown in Figures 3, 4, and 5. All phase responses $\sqrt{\angle E_{P1}^2 + \angle E_{P2}^2}$ are expressed as optical path distances (OPD) in nanometers assuming a refractive index, n, of 1.35 and using Equation (8), where λ is the central wavelength (860 nm).

$$OPD = \frac{\lambda}{4\pi n}\varphi \quad \text{(Equation 8)}$$

The same procedure was followed for the results in Figure 6. In this case, the neurons were thresholded from the background after 2D phase unwrapping via thresholding. This binary mask was resized using the size of the ROI arrays using the `imresize` function in MATLAB. Only the 5 × 5 pixels² ROIs within this binary mask were considered for the quantitative analysis in Figure 6B. Within each 1-s interval, 400 ROIs on average were used to generate the light blue and orange contours; cumulatively 9,056 ROIs from 7 dishes were used to generate the dark blue and orange contours in Figure 6B.

Figure S8 was generated by using the `pca` function in MATLAB, with pairwise comparison for the different rows. The dimension-reduced responses were extracted by matrix multiplication of the first 5 columns of the resultant score matrix and the first 5 rows of the transpose of the coefficient matrix. k-means clustering was achieved using the kmeans function in the MATLAB on the dimension-reduced responses.

Electrical stimulation and electrophysiology

A micropipette electrode (573050 suction electrodes, AM systems) was placed near a cell and connected through an electrode holder to a neuroamplifier (Model 1700, AM systems) and an analog stimulus isolator

(Model 2200, AM systems). The electrode was connected to the 'stimulus' channel of the amplifier and the current was imparted using a manually-triggered digital button, that injected 5 mA at 5 kHz for 10 ms. A part of the current output was also connected to an input of the DAQ card to synchronously record the instance of electrical stimulation. The extracellular field potentials were measured using the same setup used for electrical stimulation to generate the results in Figures 4 and 5, where the Model 1700 amplifier was operated in recording mode. The electrical signals were captured using a DAQ device (NI 6353, National Instruments). The amplifier was set to pass frequencies between 10 and 10,000 Hz with an additional notch filter at 60 Hz to reject electrical noise. The sample arm of the system was placed inside a custom Faraday cage.

QUANTIFICATION AND STATISTICAL ANALYSIS

For the results in Figure 5, the Kruskal-Wallis test was performed using the `kruskalwallis` test in MATLAB. For the results in Figures 6 and S7, the two-sample t-test was performed with unequal variance type using the `ttest2` function in MATLAB.